Microscopic study of ^{7}Li-nucleus potential*

Wen-Di Chen(陈文棣)[1] Hai-Rui Guo(郭海瑞)[2;1)] Wei-Li Sun(孙伟力)[2] Tao Ye(叶涛)[2] Yang-Jun Ying(应阳君)[2]
Yin-Lu Han(韩银录)[3] Qing-Biao Shen(申庆彪)[3]

[1]Graduate School of China Academy of Engineering Physics, Beijing 100088, China
[2]Institute of Applied Physics and Computational Mathematics, Beijing 100094, China
[3]Key Laboratory of Nuclear Data, China Institute of Atomic Energy, Beijing 102413, China

Abstract: A microscopic approach is employed to study the optical potential for the ^{7}Li-nucleus interaction system without any free parameters. It is obtained by folding the microscopic optical potentials of the constituent nucleons of ^{7}Li over their density distributions. We employ an isospin-dependent nucleon microscopic optical potential, which is based on the Skyrme nucleon-nucleon effective interaction and derived using the Green's function method, as the nucleon optical potential. The harmonic oscillator shell model is used to describe the internal wave function of ^{7}Li and obtain the nucleon density distribution. The ^{7}Li microscopic optical potential is used to predict the reaction cross-sections and elastic scattering angular distributions for the target range from ^{27}Al to ^{208}Pb and energy range below 450 MeV. Generally, the results can reproduce the measured data reasonably well. In addition, the microscopic optical potential is comparable to a global phenomenological optical potential by fitting the presently existing measured data.

Keywords: ^{7}Li microscopic optical potential, ^{7}Li elastic scattering, folding model

DOI: 10.1088/1674-1137/44/5/054109

1 Introduction

The optical potential is an usual and basic tool used in the dynamic analyses of nuclear reactions. At present, most optical potentials are phenomenological. They have several parameters, and they are determined by fitting experimental data. When the experimental data are not sufficient, it is difficult to obtain a reliable phenomenological optical potential. In contrast, the microscopic optical potential (MOP) is theoretically derived from the nucleon-nucleon interaction, it has no free parameters, and does not rely on the experimental data. Therefore, to obtain optical potentials through a microscopic approach represents a goal of nuclear physics. It is of great significance for the analyses of nuclear reactions lacking experimental data.

The studies of nuclear reactions involving a light-particle projectile or ejectile are an important part of nuclear physics and highly useful for practical applications. Thus, we have already obtained the MOPs for the nucleon [1], deuteron [2], triton [3], and ^{3,4,6}He [4-6]. In recent years, the weakly bound ^{7}Li induced reactions has been a topic of great interest. Breakup, complete and incomplete fusion, and some other reaction mechanisms were addressed by experimental and theoretical nuclear physicists [7, 8]. The ^{7}Li optical potential is required in the theoretical analyses.

To date, there are several ^{7}Li optical potentials employed to analyze the experimental data. A semi-microscopic optical potential, whose real part is generated by the double folding model and nucleon-nucleon effective interaction and whose imaginary part is in the Woods-Saxon form, is given by Woods et al. [9] and used to analyze elastic scattering data for the ^{15}N and ^{25}Mg target. Deshmukh et al. [10] provided a Wood-Saxon form optical potential, while it can only be used for ^{116}Sn. An optical potential provided by Camacho et al. [11] meets the dispersion relation of real and imaginary parts; however, it is only suitable for the ^{28}Si target. Recently, Xu et al. [12] provided a new global phenomenological optical potential (GOP) based on the present experimental data, which is applicable to a more extensive incident energy and target region.

Since the measured ^{7}Li scattering data are not sufficient to date, a ^{7}Li MOP is obtained in the present work by folding the MOPs of its internal nucleons over their density distributions. The isospin-dependent nonrealistic

Received 3 January 2020, Published online 31 March 2020
* Supported by National Natural Science Foundation of China (11705009, 11575291) and Science Challenge Project (TZ2018005)
1) E-mail: guo_hairui@iapcm.ac.cn

nucleon MOP derived using the Green's function method in our previous work [1, 13-15] is adopted to be the MOP for the constituent nucleons. The shell model is applied to construct the internal wave function and generate nucleon density distributions. The ^{7}Li elastic-scattering angular distributions and reaction cross-sections are calculated by the MOP and compared with the experimental data, and the results are calculated by the GOP [12].

This paper is organized as follows: the theoretical model and formulas of the MOP are presented in Sec. 2; the calculated results and analysis are provided in Sec. 3; the summary and conclusion are given in Sec. 4.

2 Theoretical model

The MOP for ^{7}Li is generated by the folding model [16] and expressed as

$$U(\vec{R}) = \int U_n(\vec{R}+\vec{r})\rho_n(\vec{r}) + U_p(\vec{R}+\vec{r})\rho_p(\vec{r})\mathrm{d}\vec{r}, \quad (1)$$

where

$$\int \rho_n \mathrm{d}\vec{r} = N; \quad \int \rho_p \mathrm{d}\vec{r} = Z. \quad (2)$$

U_n and U_p represent the MOPs for neutrons and protons, respectively. ρ_n and ρ_p are the density distributions of neutrons and protons in the ground state of ^{7}Li, respectively. $\vec{R}$ is the relative coordinate between the centers of mass of the target and ^{7}Li, and $\vec{r}$ is the internal coordinate of ^{7}Li.

The isospin-dependent nonrealistic nucleon MOP [1, 13-15] is adopted to be U_n and U_p for neutrons and protons, respectively. A brief introduction for it is given as follows: From the perspective of many-body theory, the nucleon optical potential is equivalent to the mass operator of the single-particle Green's function [17]. Based on the Skyrme nucleon-nucleon effective interaction SKC16 [14], which simultaneously describes nuclear matter properties, ground state properties, and neutron-nucleus scattering, the first- and second-order mass operators of the single-particle Green's function were derived through the nuclear matter and local density approximations. The real part of the nucleon MOP was denoted by the first-order mass operator, and the imaginary part of the nucleon MOP was denoted by the imaginary part of the second-order mass operator. The incident energy of the nucleon is regarded as one seventh of the incident energy of ^{7}Li.

The shell model is adopted to give an appropriate nucleon density in ^{7}Li. Because a 1p-shell model space can efficiently describe its structure [18], and as we are here only concerned with the ground-state properties of ^{7}Li, the harmonic oscillator potential is adopted to describe the mean interaction for the nucleons in ^{7}Li, and the internal Hamiltonian of ^{7}Li is expressed as

$$H_{^7\mathrm{Li}} = \sum_{i=1}^{7} T_i + \sum_{i=1}^{7} \frac{1}{2} m\omega^2 r_i^2, \quad (3)$$

where m is the nucleon mass, and r_i is coordinate of the ith nucleon in ^{7}Li relative to the center of mass of ^{7}Li. T_i represents the kinetic energy of the ith nucleon.

As the harmonic oscillator potential is used in the shell model, the ground-state wave function of ^{7}Li is expressed as

$$\Phi_{\mathrm{g.s.}} = N\mathcal{A}\left\{(\vec{r}_6\cdot\vec{r}_7)r_5 Y_1^{\mu}(\hat{r}_5)\exp\left\{-\frac{\beta}{2}\sum_{i=1}^{7} r_i^2\right\}\zeta\right\}, \quad (4)$$

where $\mathcal{A}$ is the antisymmetrization operator of the nucleons, and N is the normalization factor. ζ represents the spin and isospin part. $\Phi_{\mathrm{g.s.}}$ is determined by the parameter $\beta = m\omega/\hbar$, under the conditions of meeting antisymmetrization, spin, and parity ($I^{\pi} = 3/2^{-}$). On basis of the constraint condition,

$$\sum_{i=1}^{7} \vec{r}_i = 0, \quad (5)$$

a set of Jacobi coordinates is used to replace r_i and expressed as

$$\begin{aligned}
\vec{r}_1 &= \frac{1}{2}\vec{\xi}_1 + \frac{1}{3}\vec{\xi}_2 + \frac{1}{4}\vec{\xi}_3 + \frac{1}{3}\vec{\xi}_5 + \frac{1}{7}\vec{\xi}_6,\\
\vec{r}_2 &= -\frac{1}{2}\vec{\xi}_1 + \frac{1}{3}\vec{\xi}_2 + \frac{1}{4}\vec{\xi}_3 + \frac{1}{3}\vec{\xi}_5 + \frac{1}{7}\vec{\xi}_6,\\
\vec{r}_3 &= -\frac{2}{3}\vec{\xi}_2 + \frac{1}{4}\vec{\xi}_3 + \frac{1}{3}\vec{\xi}_5 + \frac{1}{7}\vec{\xi}_6,\\
\vec{r}_4 &= -\frac{3}{4}\vec{\xi}_3 + \frac{1}{3}\vec{\xi}_5 + \frac{1}{7}\vec{\xi}_6,\\
\vec{r}_5 &= -\frac{6}{7}\vec{\xi}_6, \quad \vec{r}_6 = \frac{1}{2}\vec{\xi}_4 - \frac{2}{3}\vec{\xi}_5 + \frac{1}{7}\vec{\xi}_6,\\
\vec{r}_7 &= -\frac{1}{2}\vec{\xi}_4 - \frac{2}{3}\vec{\xi}_5 + \frac{1}{7}\vec{\xi}_6.
\end{aligned} \quad (6)$$

The value of β is determined by

$$\left\langle r_{\mathrm{rms}}^2 \right\rangle = \left\langle \Phi_{\mathrm{g.s.}} \middle| \frac{1}{7}\sum_{i=1}^{7} r_i^2 \middle| \Phi_{\mathrm{g.s.}} \right\rangle, \quad (7)$$

where $\sqrt{\left\langle r_{\mathrm{rms}}^2 \right\rangle}$ is the nuclear matter root-mean-square radius of ^{7}Li and set as 2.50 fm, which was obtained by fitting the reaction cross-section in Ref. [19]. It is convenient to rewrite Eq. (4) as follows:

$$\Phi_{\mathrm{g.s.}} = N\mathcal{A}\{\phi_1(1234)\phi_2(5)\phi_3(67)\zeta\}, \quad (8)$$

where

$$\begin{aligned}
\phi_1(1234) &= \exp\left\{-\frac{\beta}{2}\sum_{i=1}^{4} r_i^2\right\},\\
\phi_2(5) &= r_5 Y_1^m(\hat{r}_5)\exp\left\{-\frac{\beta}{2}r_5^2\right\},\\
\phi_3(67) &= (\vec{r}_6\cdot\vec{r}_7)\exp\left\{-\frac{\beta}{2}(r_6^2 + r_7^2)\right\}.
\end{aligned} \quad (9)$$

Then, we can obtain a detailed expression for $\left\langle r^2_{\rm rms}\right\rangle$,

$$\left\langle r^2_{\rm rms}\right\rangle = \frac{A_0-2A_1-A_2+2A_3+A_4-A_5}{N_0-2N_1-N_2+2N_3+N_4-N_5}, \quad (10)$$

where

$$A_0 = \langle\phi_1(1234)\phi_2(5)\phi_3(67)|\hat{O}_A|\phi_1(1234)\phi_2(5)\phi_3(67)\rangle_\xi,$$
$$A_1 = \langle\phi_1(1234)\phi_2(5)\phi_3(67)|\hat{O}_A|\phi_1(1264)\phi_2(5)\phi_3(37)\rangle_\xi,$$
$$A_2 = \langle\phi_1(1234)\phi_2(5)\phi_3(67)|\hat{O}_A|\phi_1(5234)\phi_2(1)\phi_3(67)\rangle_\xi,$$
$$A_3 = \langle\phi_1(1234)\phi_2(5)\phi_3(67)|\hat{O}_A|\phi_1(5264)\phi_2(1)\phi_3(37)\rangle_\xi,$$
$$A_4 = \langle\phi_1(1234)\phi_2(5)\phi_3(67)|\hat{O}_A|\phi_1(1267)\phi_2(5)\phi_3(34)\rangle_\xi,$$
$$A_5 = \langle\phi_1(1234)\phi_2(5)\phi_3(67)|\hat{O}_A|\phi_1(5267)\phi_2(1)\phi_3(34)\rangle_\xi,$$

$$\hat{O}_A = \frac{1}{7}\sum_{i=1}^{7} r_i^2. \quad (11)$$

$\langle ...\rangle_\xi$ means that the coordinates $\{\vec{r}_i, i=1-7\}$ are replaced by the Jacobi coordinates $\{\vec{\xi}_i, i=1-6\}$. The formulas for N_i are the same as A_i, while $\hat{O}_A$ is replaced by $\hat{O}_N = 1$. Thus we can obtain

$$\left\langle r^2_{\rm rms}\right\rangle = \frac{12}{7\beta} \quad (12)$$

and therefore $\beta = 0.2743$ fm^{-2}.

ρ_n and ρ_p are defined as

$$\rho_{n(p)}(\vec{r}) = \left\langle \Phi_{\rm g.s.}\right| \sum_{i=1}^{7} \delta(\vec{r}-\vec{r}_i)\delta_{\tau_{n(p)},\tau_i} \left|\Phi_{\rm g.s.}\right\rangle, \quad (13)$$

where τ_i is the isospin of ith nucleon. τ_n and τ_p are the isospins of the neutron and proton, respectively. It would be convenient to calculate ρ_i first, whose formula is the same as Eq. (10), while only $\hat{O}_A$ is replaced by $\hat{O}_{\rho,i} = \delta(\vec{r}-\vec{r}_i)$. $\rho_p = \rho_1+\rho_2+\rho_5$, $\rho_n = \rho_3+\rho_4+\rho_6+\rho_7$, and they have analytical expressions as

$$\rho_{n(p)}(\vec{r}) = \left(a_{n(p)} + b_{n(p)}r^2\right)\exp\left(-\frac{7}{6}\beta r^2\right), \quad (14)$$

where $a_n = 0.0921$ fm^{-3}, $a_p = 0.0621$ fm^{-3}, $b_n = 0.0081$ fm^{-5} and $b_p = 0.0076$ fm^{-5}. The density distributions are plotted in Fig. 1.

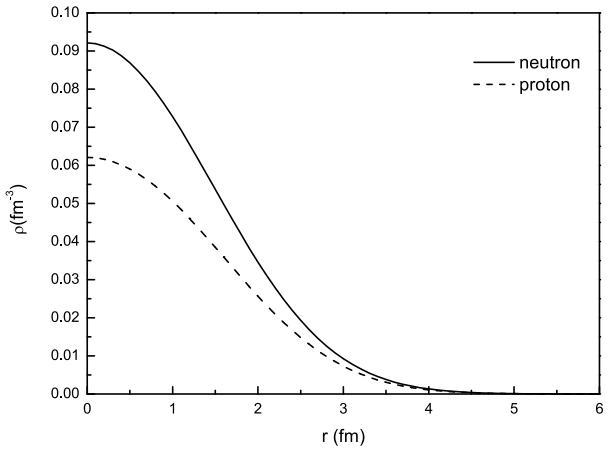

Fig. 1. Neutron (ρ_n) and proton (ρ_p) density distributions.

3 Calculated results and analysis

The MOP for the ^{7}Li+^{58}Ni collision system at incident ^{7}Li energies of 10, 100, and 300 MeV is shown in Fig. 2 as an example. The depth of the real part (V) decreases with the increase of the radius and energy. However, the depth of the imaginary part (W) increases a little first and decreases as the radius increases at EL = 10, 100 MeV, while it decreases monotonously with the increase of the radius at a higher incident energy, 300 MeV. This means the contribution of W changes from the dominant surface absorption to the volume absorption as the incident energy increases. The real part of the spin-orbit potential

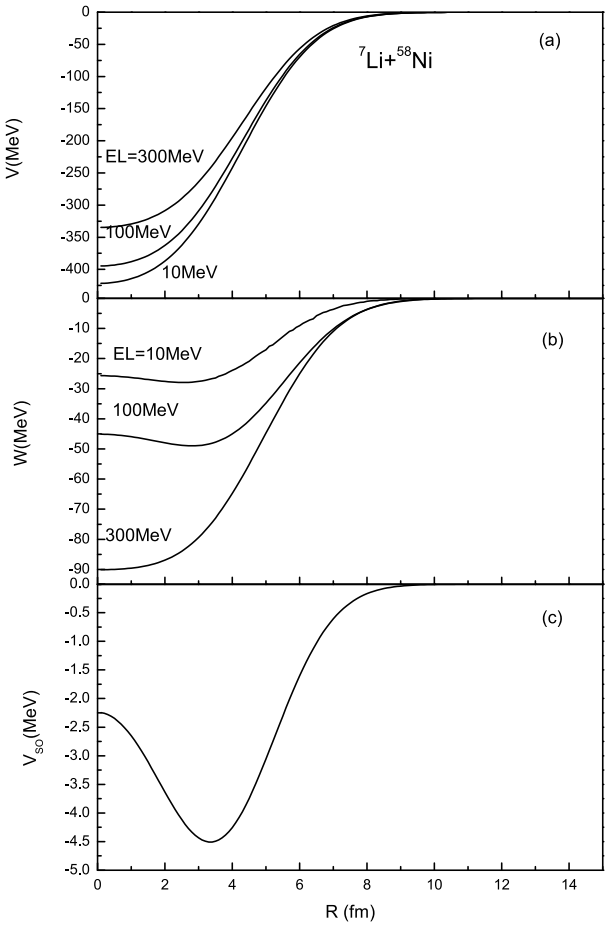

Fig. 2. MOP for ^{7}Li+^{58}Ni system (a) real part (V), (b) imaginary part (W) and (c) real part of spin-orbit potential ($V_{\rm so}$).

$V_{\rm so}\vec{s}\cdot\vec{l}$ is likewise obtained by the folding model, and $V_{\rm so}$ is shown in Fig. 2, while the imaginary part of the spin-orbit potential is omitted as it is usually very small.

The ^{7}Li elastic-scattering angular distributions and reaction cross-sections are predicted using the MOP. Comparisons are made with experimental data and the results

calculated by the GOP [12].

Figure 3 shows the elastic-scattering angular distribution for ^{27}Al target at incident energies from 6.0 to 24.0 MeV. The result calculated by the MOP is in good agreement with experimental data [20, 21] except for the underestimation at EL = 11.0 MeV for large angles. In addition, the MOP result fits the experimental data slightly better than the result calculated by the GOP [12] below 14 MeV at larger angles.

The calculated elastic-scattering angular distribution for ^{58}Ni target at incident energies from 14.22 MeV to 42.0 MeV is plotted in Fig. 4. The MOP efficiently reproduces the experimental data [22-24], except the slight underestimation above 70° at 16.25 MeV and 18.28 MeV, where the GOP performs slightly better.

The elastic-scattering angular distributions for ^{65}Cu at incident energy 25.0 MeV and ^{89}Y at incident energy 60.0 MeV are shown in Fig. 5. For ^{65}Cu, the theoretical result from the MOP is lower than the measured values [25] above 70°. Reasonable agreement with the experimental data [26] is obtained for ^{89}Y.

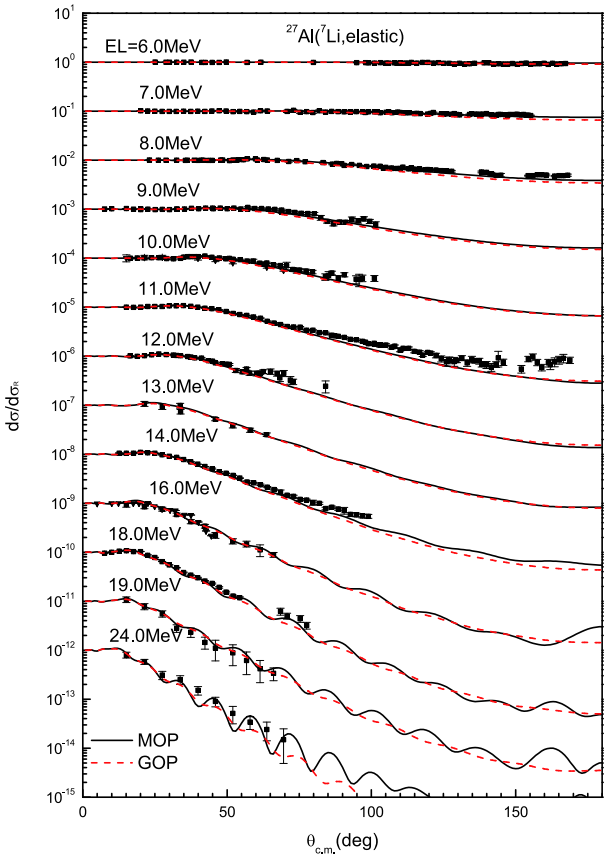

Fig. 3. (color online) Calculated elastic-scattering angular distributions in Rutherford ratio for ^{27}Al compared with experimental data [20, 21]. Solid and dashed lines denote results calculated by MOP and the GOP [12], respectively. Graph results from top to bottom are multiplied 10^{0}, 10^{-1}, 10^{-2}, respectively.

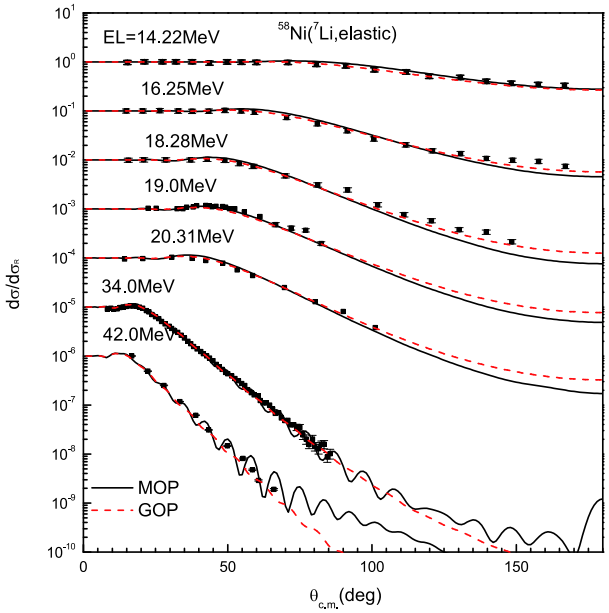

Fig. 4. (color online) Same as Fig. 3 for ^{58}Ni. Experimental data are taken from Refs. [22-24]. Results from top to bottom are multiplied by 10^{0}, 10^{-1}, 10^{-2}, respectively.

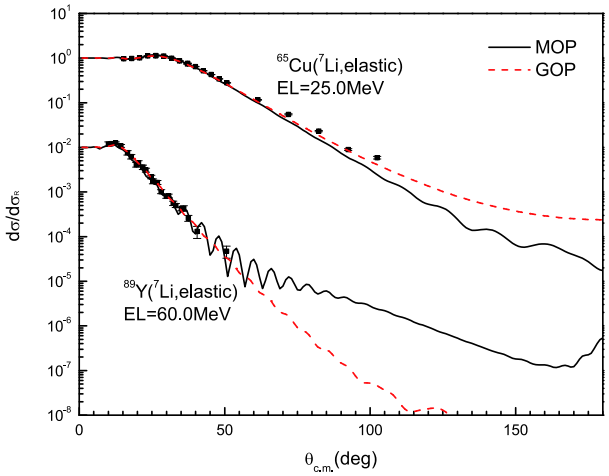

Fig. 5. (color online) Same as Fig. 3 for ^{65}Cu and ^{89}Y. Experimental data are taken from Refs. [25, 26]. The data for ^{89}Y are multiplied by 10^{-2}.

Figure 6 shows the elastic-scattering angular distribution for the ^{116}Sn target at incident energies from 18.0 MeV to 35.0 MeV. The calculated result from the MOP is in good agreement with experimental data [10] except at incident energies 22.0, 24.0, and 26.0 MeV at large angles. The MOP reproduces the measurements slightly better than the GOP at relatively lower energies.

The calculated elastic-scattering angular distribution for ^{138}Ba targets is compared with experimental data [27, 28] in Fig. 7. When the scattering angles are less than 80°, good agreement with experimental data is obtained

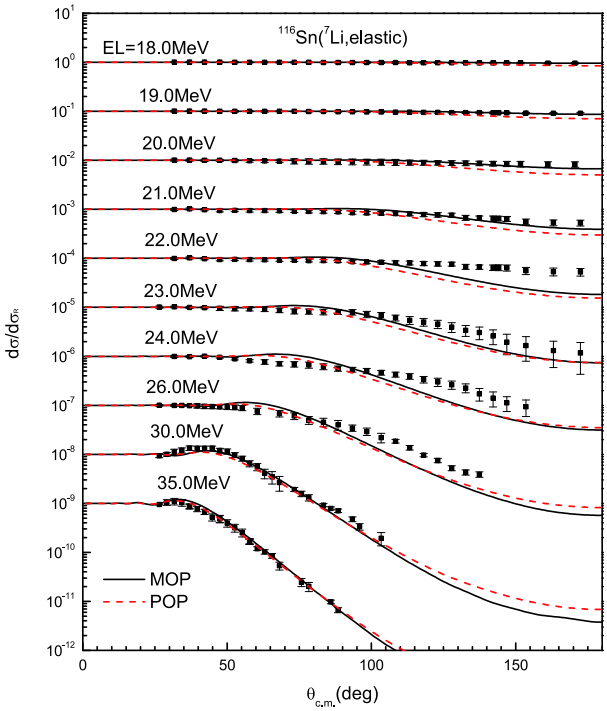

Fig. 6. (color online) Same as Fig. 3 for ^{116}Sn. Experimental data are taken from Ref. [10]. Results from top to bottom are multiplied by 10^{0}, 10^{-1}, 10^{-2}, respectively.

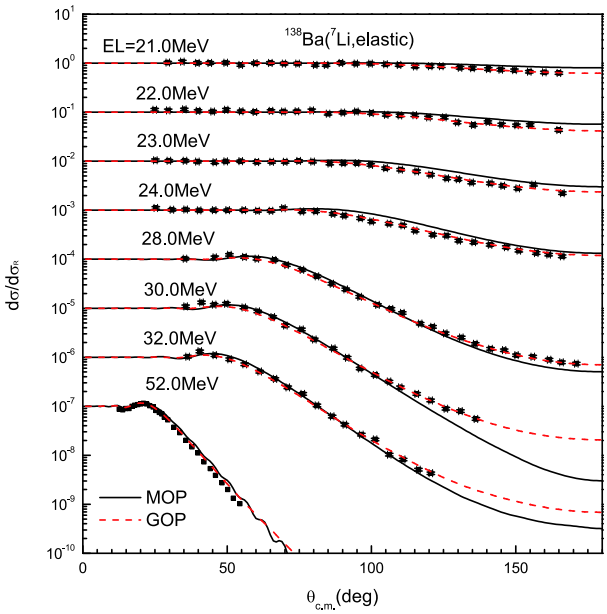

Fig. 7. (color online) Same as Fig. 3 for ^{138}Ba. The experimental data are taken from Refs. [27, 28]. The results from top to bottom are multiplied respectively by 10^{0}, 10^{-1}, 10^{-2}.

for the MOP. The GOP works better at larger angles.

In Fig. 8, the calculated elastic-scattering angular distribution for ^{208}Pb is shown from 27.0 MeV to 52.0 MeV. The MOP result is in satisfying agreement with experimental data [29-32] and comparable to the GOP result in

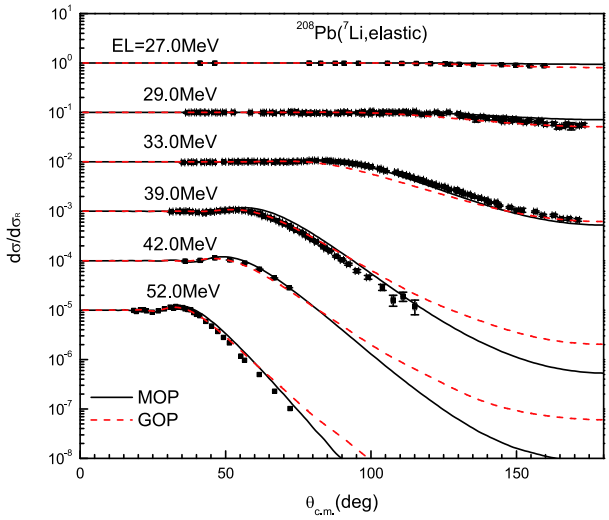

Fig. 8. (color online) Same as Fig. 3 for ^{208}Pb. Experimental data are taken from Refs. [29-32]. Results from top to bottom are multiplied by 10^{0}, 10^{-1}, 10^{-2}, respectively

fitting the measured data, except for the case at 39 MeV above 70°.

Figure 9 shows the elastic-scattering angular distribution at some specific scattering angles for ^{27}Al target. The calculated result by the MOP is slightly larger than that by the GOP at incident energies below 15 MeV and has a little better agreement with the measured values [33-36] when $EL\leqslant 9$ MeV. However, all calculated results from the MOP and the GOP underestimate the experimental data [37] at incident energies from 9 MeV to 11 MeV for large angles.

The reaction cross-sections of ^{7}Li-induced reactions on ^{13}C, ^{27}Al, ^{28}Si, ^{64}Zn, ^{nat}Cu, ^{116}Sn, ^{138}Ba, and ^{208}Pb are also calculated and shown in Fig. 10 and Fig. 11. Figure 10 presents the results for ^{13}C, ^{28}Si, ^{nat}Cu and ^{208}Pb. The theoretical result for ^{13}C is within the measurement error range [38]. The MOP result for ^{28}Si is in good agreement with experimental data [39-43] below 30 MeV; however, it becomes a little larger from 90 MeV to 200 MeV. The reaction cross-section for ^{nat}Cu is obtained by averaging the reaction cross-sections for ^{63}Cu and ^{65}Cu over the natural abundance. The MOP result is in good agreement with the experimental data [44] except for the energy point of 160 MeV. The MOP result for ^{208}Pb reproduces the experimental data [30, 45] reasonably well below 70 MeV; however, it yields an underestimation at 300 MeV. Figure 11 shows that the MOP reproduces experimental data for ^{27}Al [21, 46], ^{64}Zn [47], ^{116}Sn [10], and ^{138}Ba [28] well. The MOP results are comparable to the GOP results in fitting the measured reaction cross-sections except for ^{208}Pb.

The application of the MOP to the prediction of ^{7}Li

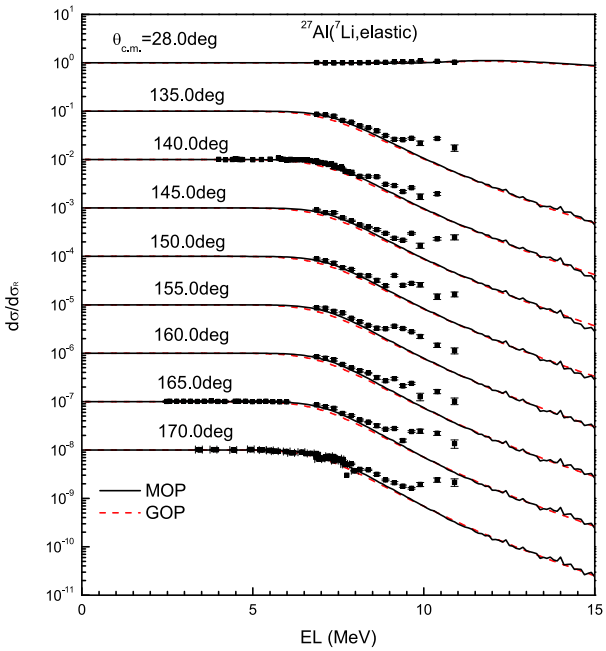

Fig. 9. (color online) Calculated elastic-scattering angular distributions in Rutherford ratio for ^{27}Al at some scattering angles compared with experimental data [33-37]. Solid and dashed lines denote results calculated by MOP and GOP [12], respectively. The results from top to bottom are multiplied by 10^{0}, 10^{-1}, 10^{-2}, respectively.

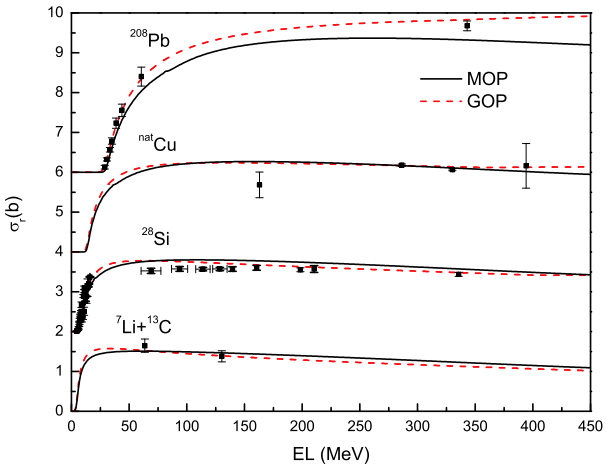

Fig. 10. (color online) Reaction cross-sections calculated by MOP compared with experimental data for ^{13}C [38], ^{28}Si [39-43], ^{nat}Cu [44] and ^{208}Pb [30, 45] and results calculated by GOP [12]. Data are shifted upwards by adding 0, 2, 4 and 6 b, respectively. Solid and dashed lines denote results calculated by MOP and GOP, respectively.

elastic scattering from light target nuclei was attempted. The elastic-scattering angular distribution for ^{16}O is calculated and compared with experimental data [48-51], as shown in Fig. 12. The theoretical result from the MOP is only consistent with the magnitude of measured data in forward angles and gives an overestimation in relatively

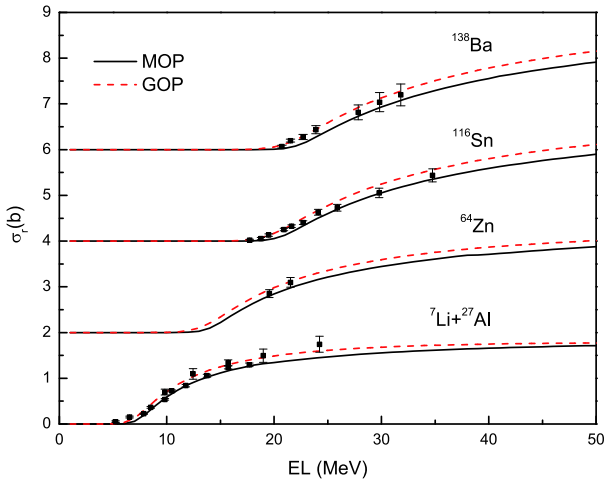

Fig. 11. (color online) Same as Fig. 10 for ^{27}Al, ^{64}Zn, ^{116}Sn, and ^{138}Ba. Experimental data are taken from Refs. [10, 21, 28, 46, 47].

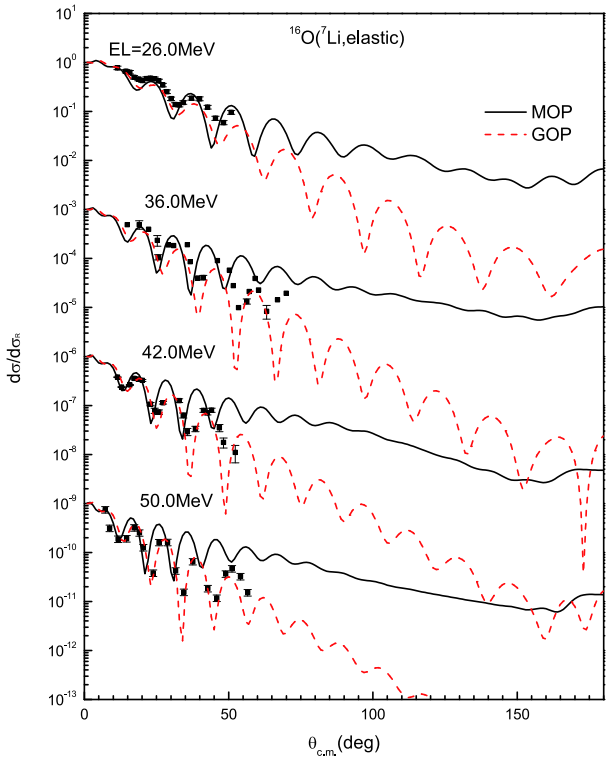

Fig. 12. (color online) Same as Fig. 3, for ^{16}O. Experimental data are taken from Refs. [48-51]. Results from top to bottom are multiplied by 10^{0}, 10^{-3}, 10^{-6}, and 10^{-9}, respectively.

larger angles. Therefore, the MOP is not suitable for light nuclei. On the one hand, it may be interpreted that the Negele's nuclear density [52] adopted to calculate the nucleon MOP [1, 13-15] is not suitable for light nuclei. On the other hand, a light nucleus, such as ^{16}O, has unique structure characteristics and reaction mechanisms [53, 54], which may also lead to discrepancy between the MOP results and measured values.

Furthermore, some discrepancies between the calculated and measured elastic-scattering angular distributions appear at relatively larger angles, such as the case for ^{138}Ba target at 28.0 MeV. To investigate how to improve the MOP to provide a better global agreement with experimental data, the notch perturbation method [55, 56] is employed to analyze the sensitivity of the calculated elastic scattering angular distributions to the optical potential. The perturbation is performed by setting V, W, or V_{so} to zero in a region of width 0.5 fm centered at radius R. The scattering sensitivity is assessed by χ^2/χ_0^2, where the χ^2 and χ_0^2 are the chi-squares corresponding to the perturbed and original potentials, respectively. χ_0^2 is calculated by

$$\chi_0^2 = \frac{1}{N_\theta}\sum_{i=1}^{N}\left[\frac{\sigma_0^T(\theta_i)-\sigma^E(\theta_i)}{\Delta\sigma^E(\theta_i)}\right]^2, \quad (15)$$

where N_θ is the angle numbers of the experimental elastic-scattering angular distributions for ^{7}Li+^{138}Ba at EL = 28.0 MeV. $\sigma_0^T(\theta_i)$, $\sigma^E(\theta_i)$ and $\Delta\sigma^E(\theta_i)$ represent the theoretical value without perturbation, experimental value, and experimental error for the ith measured scattering angle, respectively. The theoretical value with perturbation, $\sigma^T(\theta_i)$, is used to calculate χ^2 in the same method.

Figure 13 shows the MOP for the ^{7}Li+^{138}Ba system at EL = 28.0 MeV and χ^2/χ_0^2. χ^2/χ_0^2 for V_{so} of the MOP approximately remains at unity, hence it is acceptable to ignore the impact from changing V_{so} and focus on only V and W. The peaks of χ^2/χ_0^2 are located mainly in the surface interaction region $6 < R < 12$ fm.

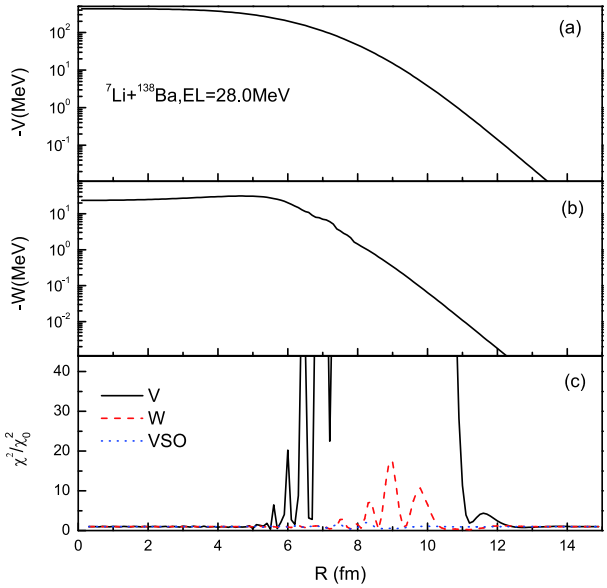

Fig. 13. (color online) Notch perturbation analysis of MOP for ^{7}Li+^{138}Ba reaction at EL = 28.0 MeV, (a) V of MOP; (b) W of MOP; (c) radial sensitivity of elastic scattering to MOP. Solid, dashed, and dotted curves in (c) represent results of perturbing V, W, and V_{so}, respectively.

We adjust the V and W of the MOP in the sensitive region $6 < R < 12$ fm by multiplying N_R and N_I, respectively, and calculate the corresponding χ^2/χ_0^2. It can be seen in Figure 14 shows that a better agreement with experimental data at large angles is obtained when N_R = 0.89 and N_I = 1.00. This implies that a weaker real part in the surface region of the MOP may be more suitable for reproducing the measured data. In contrast, a smaller χ^2 is obtained when N_R = 1.00 and N_I = 1.89, which means that a stronger imaginary part in the surface region may perform better. A correction of the MOP results is expected from the breakup effect, which is not considered in the folding model, as it onlny provides a repulsive contribution to the real part and an absorptive contribution to the imaginary part in the surface region.

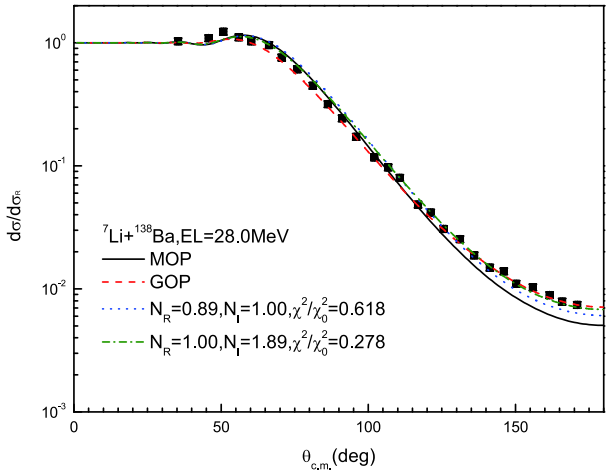

Fig. 14. (color online) Calculated elastic-scattering angular distributions in Rutherford ratio for ^{138}Ba at EL = 28.0 MeV. Solid, dashed, dotted, and dash-dotted lines denote results calculated by MOP, GOP [12], MOP with adjusted V and MOP with adjusted W, respectively. Adjustments of V and W are made only within sensitive region $6 < R < 12$ fm.

4 Summary and conclusion

The ^{7}Li microscopic optical potential without any free parameters is obtained by the folding model. The internal wave function of ^{7}Li is obtained by the shell model, and a nucleon MOP base on the Skyrme nucleon-nucleon effective interaction is adopted. The reaction cross-sections and elastic-scattering angular distributions for target from ^{27}Al to ^{208}Pb at incident energies below 450 MeV are calculated by the ^{7}Li microscopic optical potential. Generally, reasonable agreement with the experimental data is obtained, and the MOP is comparable to the GOP in reproducing the measurements in numerous cases. However, some discrepancies between the calculated and

measured elastic-scattering angular distributions occur at relatively larger angles. The reason is analyzed, and it is found that the MOP can be improved by adding a repulsive contribution to the real part and an absorptive contribution to the imaginary part in the surface region, which may be achieved by considering the breakup effect. This will be the subject of our future study.

References

1 Q. B. Shen, Y. L. Han, and H. R. Guo, Phys. Rev. C, **80**: 024604 (2009)
2 H. R. Guo, Y. Y. Xu, Y. L. Han *et al*., Phys. Rev. C, **81**: 044617 (2010)
3 H. R. Guo, Y. L. Xu, H. Y. Liang *et al*., Nucl. Phys. A, **922**: 84-98 (2014)
4 H. R. Guo, Y. Zhang, Y. L. Han *et al*., Phys. Rev. C, **79**: 064601 (2009)
5 H. R. Guo, Y. L. Xu, H. Y. Liang *et al*., Phys. Rev. C, **83**: 064618 (2011)
6 H. R. Guo, H. Y. Liang, Y. L. Xu *et al*., Phys. Rev. C, **95**: 034614 (2017)
7 V. V. Parkar, S. K. Sharma, R. Palit *et al*., Phys. Rev. C, **97**: 014607 (2018)
8 M. S. Gautam, N. Grover, and M. K. Sharma Eur, Phys. J. A, **53**: 12 (2017)
9 C. L. Woods, B. A. Brown, and N. A. Jelley, J. Phys. G Nucl. Phys., **8**: 1699-1719 (1982)
10 N. N. Deshmukh, S. Mukherjee, B. K. Nayak *et al*., Eur. Phys. J. A, **47**: 118 (2011)
11 C. A. Gómez, P. R. S. Gomes, and J. Lubian, Phys. Rev. C, **82**: 067601 (2010)
12 Y. L. Xu, Y. L. Han, J. Q. Hu *et al*., Phys. Rev. C, **97**: 014615 (2018)
13 Y. L. Xu, H. R. Guo, Y. L. Han *et al*., J. Phys. G: Nucl. Part. Phys., **41**: 015101 (2014)
14 Y. L. Xu, H. R. Guo, Y. L. Han *et al*., EPJ Web Conf., **146**: 12021 (2017)
15 Y. L. Xu, H. R. Guo, Y. L. Han *et al*., Phys. Rev. C, **96**: 024621 (2017)
16 G. R. Satchler, Nucl. Phys. A, **329**: 233-258 (1979)
17 J. S. Bell and E. J. Squires, Phys. Rev. Lett., **3**: 96-97 (1959)
18 J. N. Gu, L. R. Dai, and C. H. Zhang, High Energy Phys. Nucl. Phys., **20**: 185-192 (1996)
19 I. Tanihata, H. Hamagaki, O. Hashimoto *et al*., Phys. Rev. Lett., **55**: 2676-2679 (1985)
20 J. M. Figueira, D. Abriola, J. O. Fernández Niello *et al*., Phys. Rev. C, **73**: 054603 (2006)
21 K. Kalita, S. Verma, R. Singh *et al*., Phys. Rev. C, **73**: 024609 (2006)
22 C. W. Glover, R. I. Cutler, and K. W. Kemper, Nucl. Phys. A, **341**: 137-148 (1980)
23 A. Andronic, Nucl. Phys. A, **661**: 333-336 (1999)
24 K. Zerva, A. Pakou, N. Patronis *et al*., Eur. Phys. J. A, **48**: 102 (2012)
25 A. Shrivastava, A. Navin, N. Keeley *et al*., Phys. Lett. B, **633**: 463-468 (2006)
26 R. Wadsworth, M. D. Cohler, M. J. Smithson *et al*., J. Phys. G: Nucl. Phys., **9**: 1237-1244 (1983)
27 P. D. Clark, T. R. Ophel, J. S. Eck *et al*., Nucl. Phys. A, **349**: 258-270 (1980)
28 A. M. M. Maciel, P. R. S. Gomes, J. Lubian *et al*., Phys. Rev. C, **59**: 2103-2107 (1999)
29 V. V. Parker, V. Jha, B. J. Roy *et al*., Phys. Rev. C, **78**: 021601 (2008)
30 N. Keeley, S. J. Bennett, N. M. Clarke *et al*., Nucl. Phys. A, **571**: 326-336 (1994)
31 D. Gupta, C. Samanta, A. Chatterjee *et al*., Nucl. Phys. A, **683**: 3-20 (2001)
32 A. F. Zeller, D. C. Weisser, T. R. Ophel *et al*., Nucl. Phys. A, **332**: 515-524 (1979)
33 J. Räisänen and E. Rauhala, Nucl. Instrum. Methods Phys. Res., Sect. B, **73**: 439-442 (1993)
34 E. Rauhala and J. Räisänen, J. Appl. Phys., **75**: 642-644 (1994)
35 A. Nurmela, E, Rauhala, and J. Räisänen, Nucl. Instrum. Methods Phys. Res., Sect. B, **155**: 211-220 (1999)
36 M. Mayer, B. Diaz-Herrera, and M. Schneider, Nucl. Instrum. Methods Phys. Res., Sect. B, **207**: 263-267 (2003)
37 D. Abriola, P. Carnelli, A. Arazi *et al*., Nucl. Instrum. Methods Phys. Res., Sect. B, **268**: 1793-1796 (2010)
38 F. Carstoiu, L. Trache, R. E. Tribble *et al*., Phys. Rev. C, **70**: 054610 (2004)
39 R. E. Warner, R. A. Patty, P. M. Voyles *et al*., Phys. Rev. C, **54**: 1700-1709 (1996)
40 Y. Sobolev, A. Budzanowski, E. Bialkowski *et al*., Bull. Russ. Acad. Sci.: Phys., **69**: 1790-1795 (2005)
41 A. Pakou, K. Rusek, N. Alamanos *et al*., Phys. Rev. C, **76**: 054601 (2007)
42 A. Pakou, K. Rusek, N. Alamanos *et al*., Eur. Phys. J. A, **39**: 187-194 (2009)
43 A. Musumarra, P. Figueira, F. De Luca *et al*., Nucl. Instrum. Methods Phys. Res., Sect. A, **612**: 399-406 (2010)
44 M. G. Saint-Laurent, R. Anne, D. Bazin *et al*., Z. Physik A - Atomic Nuclei, **332**: 457-465 (1989)
45 J. M. Figueira, J. O. Fernández Niello, A. Arazi *et al*., Phys. Rev. C, **81**: 024613 (2010)
46 E. A. Benjamim, A. Lépine-Szily, D. R. Mendes Junior *et al*., Phys. Lett. B, **647**: 30-35 (2007)
47 P. R. S. Gomes, M. D. Rodríguez, G. V. Martí *et al*., Phys. Rev. C, **71**: 034608 (2005)
48 B. Guo, Z. H. Li, M. Lugaro *et al*., Astrophys. J., **756**: 193 (2012)
49 P. Schumacher, N. Ueta, H. H. Duhm *et al*., Nucl. Phys. A, **212**: 573-599 (1973)
50 A. T. Rudchik, K. W. Kemper, A. A. Rudchik *et al*., Phys. Rev. C, **75**: 024612 (2007)
51 J. Cook, K. W. Kemper, P. V. Drumm *et al*., Phys. Rev. C, **30**: 1538-1544 (1984)
52 J. W. Negele, Phys. Rev. C, **1**: 1260-1321 (1970)
53 X. J. Sun, W. J. Qu, J. F. Duan *et al*., Phys. Rev. C, **78**: 054610 (2008)
54 J. S. Zhang, Statistical Theory of Neutron Induced Reactions of Light Nuclei, 2nd ed.(in Chinese), Science Press, 2015 ISBN: 978-7-03-043975-8
55 P. J. Moffa, C. B. Dover, and J. P. Vary, Phys. Rev. C, **13**: 147-155 (1976)
56 J. G. Cramer and R. M. DeVries, Phys. Rev. C, **22**: 91-96 (1980)